Title: White matter microstructure across the adult lifespan: A mixed longitudinal and cross-sectional study using advanced diffusion models and brain-age prediction

Authors: Dani Beck[1,2,3], Ann-Marie de Lange[1,2,4], Ivan I. Maximov[1,2], Geneviève Richard[2], Ole A. Andreassen[2,5], Jan E. Nordvik[6], Lars T. Westlye[1,2,5]

[1] Department of Psychology, University of Oslo, Oslo, Norway

[2] NORMENT, Division of Mental Health and Addiction, Oslo University Hospital & Institute of Clinical Medicine, University of Oslo, Oslo, Norway

[3] Sunnaas Rehabilitation Hospital HT, Nesodden, Oslo, Norway

[4] Department of Psychiatry, University of Oxford, Warneford Hospital, Oxford, UK

[5] KG Jebsen Centre for Neurodevelopmental Disorders, University of Oslo, Oslo, Norway

[6] CatoSenteret Rehabilitation Center, Son, Norway

* Corresponding authors: Dani Beck (dani.beck@psykologi.uio.no) & Lars T. Westlye (l.t.westlye@psykologi.uio.no), Department of Psychology, University of Oslo, PO Box 1094 Blindern, 0317 OSLO, Norway, phone: +47 22845000, Fax: +47 22845001

Declarations of interest: none.

Conflict of interest: none.

Abstract

The macro- and microstructural architecture of human brain white matter undergo substantial alterations throughout development and ageing. Most of our understanding of the spatial and temporal characteristics of these lifespan adaptations come from magnetic resonance imaging (MRI), including diffusion MRI (dMRI), which enables visualization and quantification of brain white matter with unprecedented sensitivity and detail. However, with some notable exceptions, previous studies have relied on cross-sectional designs, limited age ranges, and diffusion tensor imaging (DTI) based on conventional single-shell dMRI. In this mixed cross-sectional and longitudinal study (mean interval: 15.2 months) including 702 multi-shell dMRI datasets, we combined complementary dMRI models to investigate age trajectories in healthy individuals aged 18 to 94 years (57.12% women). Using linear mixed effect models and machine learning based brain age prediction, we assessed the age-dependence of diffusion metrics, and compared the prediction accuracy of six different diffusion models, including diffusion tensor (DTI) and kurtosis imaging (DKI), neurite orientation dispersion and density imaging (NODDI), restriction spectrum imaging (RSI), spherical mean technique multi-compartment (SMT-mc), and white matter tract integrity (WMTI). The results showed that the age slopes for conventional DTI metrics (fractional anisotropy [FA], mean diffusivity [MD], axial diffusivity [AD], radial diffusivity [RD]) were largely consistent with previous research, and that the highest performing advanced dMRI models showed comparable high age sensitivity to conventional DTI. Linear mixed effects models and brain age prediction showed that the 'FA fine' metric of the RSI model and 'orientation dispersion' (OD) metric of the NODDI model showed highest sensitivity to age. The results indicate that advanced diffusion models (DKI, NODDI, RSI, SMT mc, WMTI) yield the capability of detecting sensitive measures of age-related microstructural changes of white matter in the brain that complement and extend the contribution of conventional DTI.

Key words: ageing, white matter, multi-shell, longitudinal, diffusion, brain age

1. Introduction

The architecture of human brain white matter undergoes constant remodelling throughout the lifespan. Age-related trajectories of white matter macro- and microstructure typically reflect increases during childhood, adolescence and early adulthood (Krogsrud et al., 2016; Westlye et al., 2010), and subsequent deterioration and degradation in senescence (Cox et al., 2016; Davis et al., 2009). While the field has primarily been dominated by cross-sectional studies, which by design lack information on individual trajectories (Schaie, 2005), longitudinal studies in the last decade have shown corresponding white matter changes in both development and ageing (Barrick et al., 2010; Bender et al., 2016; Bender & Raz, 2015; de Groot et al., 2016; Likitjaroen et al., 2012; Racine et al., 2019; Sexton et al., 2014; Storsve et al., 2016; Teipel et al., 2010). However, studies that have evaluated individual differences in change across a wide age range are rare (Bender et al., 2016).

White matter properties have commonly been investigated using traditional diffusion tensor imaging (DTI), and DTI based fractional anisotropy (FA) as well as mean (MD), axial (AD), and radial (RD) diffusivity are highly sensitive to age (Cox et al., 2016; Sexton et al., 2014; Westlye et al., 2010; Yap et al., 2013). However, limitations of conventional DTI metrics such as underestimation of diffusion restriction in voxels within crossing fibres (Pines et al., 2020) have motivated continued development of more advanced diffusion MRI (dMRI) models including *diffusion kurtosis imaging* (DKI) (Jensen et al., 2005), which was developed to address the restricted diffusion or non-Gaussianity in the diffusion signal (Jensen et al., 2005); *neurite orientation dispersion and density imaging* (NODDI) (Zhang et al., 2012), which models three types of microstructural environments: intra-cellular, extra-cellular, and an isotropic water pool responsible for the space occupied by cerebrospinal fluid (CSF); *white matter tract integrity* (WMTI) (Chung et al., 2018; Fieremans et al., 2011), which derives microstructural characteristics from intra- and extra-axonal environments (Chung et al., 2018; Fieremans et al., 2011); *restriction spectrum imaging* (RSI) (White et al., 2013), which applies linear mixture modelling to resolve a spectrum of length scales while simultaneously acquiring geometric information (White et al., 2013); and *spherical mean technique multi-compartment* (SMT mc) (Kaden, Kruggel, et al., 2016), a method for microscopic diffusion anisotropy imaging that is unconfounded by effects of fibre crossings and orientation dispersion (Kaden, Kelm, et al., 2016). Usually based on multi-shell acquisitions with several diffusion weightings (Andersson & Sotiropoulos, 2015; Jbabdi et al., 2012), these models can be broadly split into "signal" and "tissue" models (D. C. Alexander et al., 2019). Signal representations, such as DTI and DKI, describe the diffusion signal behaviour in a voxel without assumptions about underlying tissue, but the estimated parameters lack specificity, meaning its characterisation of

tissue microstructure remains indirect (Jelescu & Budde, 2017). Tissue models (NODDI, RSI, SMT-mc, and WMTI) however, are assumed to provide a geometry of underlying tissue (Novikov et al., 2019), and thus may provide higher biological specificity and more precise measures of white matter microstructure and architecture (Jelescu & Budde, 2017; Novikov et al., 2019; Pines et al., 2020). Despite tissue models being designed to increase specificity, they also require assumptions about the underlying microstructure, and these assumptions may at times be invalid.

Building on the opportunities from big data in neuroimaging (S. M. Smith & Nichols, 2018), age related brain changes have recently been investigated using machine learning techniques such as brain age prediction; the estimation of the 'biological' age of a brain based on neuroimaging data (J. H. Cole et al., 2018; de Lange et al., 2019; Kaufmann et al., 2019; Franke et al., 2010; Richard et al., 2018). Predicting the age of a brain, and subsequently looking at the disparity between predicted and chronological age, can identify important individualised markers of brain integrity that may reveal risk of neurological and/or neuropsychiatric disorders (Kaufmann et al., 2019). While brain age prediction has grown more popular in recent years, most studies have used grey matter features for brain age prediction, while only few have exclusively (Tønnesen et al., 2018), or partly (James H Cole, 2019; Maximov et al., 2020; Richard et al., 2018; S. M. Smith, Elliott, et al., 2019; S. M. Smith, Vidaurre, et al., 2019) utilised dMRI. However, the brain-age prediction accuracy of advanced diffusion models such as RSI and NODDI are not known.

Including cross-sectional and longitudinal data obtained from 573 healthy subjects (with 702 multi-shell dMRI datasets) aged 18-94 years, the aim of the current study was to estimate age trajectories and compare the age sensitivity of conventional (DTI) and advanced (DKI, NODDI, RSI, SMT mc, and WMTI) diffusion models based on multi-shell acquisition. First, we estimated each of the diffusion metrics across the age range. Based on previous findings using conventional DTI metrics, we predicted curvilinear global trajectories with both conventional and advanced dMRI models. Secondly, we utilised three separate methods to compare the age-sensitivity of the diffusion models: i) we used linear mixed effect models including age, sex, and timepoint, ii) for each model, we ran fits with and without age terms and compared the fit likelihood values using Wilk's theorem (Wilks, 1938), iii) we used machine learning to predict age based on the diffusion metrics, and compared the prediction accuracy of the models. We expected all metrics to be highly age-sensitive and for longitudinal evidence to support age-related white matter microstructural changes present in individuals after one follow-up session (mean interval = 15.2 months, SD = 3.48). Thirdly, we looked at the derivatives of each function of the linear mixed effects models' age curve to identify the

point of change in trajectory for each diffusion metric. We expected advanced dMRI metrics to reveal changes at points in line with previous research.

2. Methods and material

2.1. Description of sample

The initial sample included 754 multi-shell datasets of healthy subjects from two integrated studies; the Tematisk Område Psykoser (TOP) (Tønnesen et al., 2018) and StrokeMRI (Richard et al., 2018). Following the removal of 52 datasets after quality checking (QC, see section 2.4), the final sample comprised 702 scans from 573 individuals, including longitudinal data (two time-points with 15.2 months interval) for 129 of the participants. Demographic information is summarised in Table 1 and Figure 1.

Exclusion criteria included neurological and mental disorders, and previous head trauma. Ethical guidelines followed those in line with the Declaration of Helsinki. The study has been approved by the Regional Ethics Committee and all participants provided written informed consent.

Table 1. Demographics of descriptive statistics pertaining to the study sample. N refers to datasets.

	Age		
	Mean ± SD	Min	Max
Full (mixed) sample (n = 702)	50.86 ± 16.61	18.52	94.67
Male (301, 42.88%)	49.45 ± 17.48	18.52	92.05
Female (401, 57.12%)	51.92 ± 15.86	18.63	94.67
Cross-sectional sample (n = 444)	47.61 ± 16.59	18.52	94.67
Male (214, 48.20%)	46.75 ± 16.71	18.52	92.05
Female (230, 51.80%)	48.57 ± 16.51	18.63	94.67
Longitudinal sample (n = 258)	56.60 ± 15.03	20.30	85.82
Male (44, 35.11%)	55.72 ± 17.78	20.30	85.82
Female (85, 65.89%)	55.65 ± 13.70	23.37	80.62

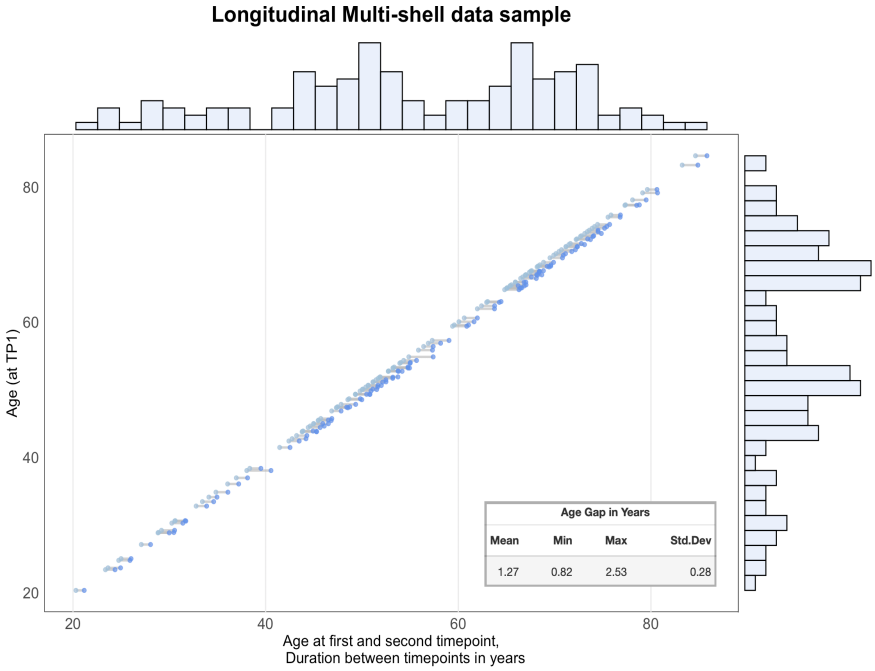

Figure 1. Interval between timepoint 1 and timepoint 2 for complete longitudinal sample, n = 258 (129 subjects). Histogram representing density of data points.

2.2. MRI acquisition

Imaging was performed at Oslo University Hospital on a General Electric Discovery MR750 3T scanner with a 32-channel head coil. dMRI data were acquired with a spin echo planar imaging (EPI) sequence with the following parameters: TR/TE/flip angle: 8,150 ms/83.1 ms/90°, FOV: 256 × 256 mm, slice thickness: 2 mm, in-plane resolution: 2 mm. We obtained 10 volumes of *b* value = *0* diffusion weighted data along 60 (b = 1000 s/mm^2) and 30 (b = 2000 s/mm^2) diffusion weighted volumes. In addition, 7 *b* value = 0 volumes with reversed phase-encoding direction were acquired for correction of susceptibility distortions.

2.3. Diffusion MRI processing

Processing steps followed a previously described pipeline (Maximov et al., 2019), including noise correction (Veraart et al., 2016), Gibbs ringing correction (Kellner et al., 2016), corrections for susceptibility induced distortions, head movements and eddy current induced distortions using topup (http://fsl.fmrib.ox.ac.uk/fsl/fslwiki/topup) and eddy (http://fsl.fmrib.ox.ac.uk/fsl/fslwiki/eddy) (Andersson & Sotiropoulos, 2016). Isotropic smoothing was carried out with a Gaussian kernel of 1 mm^3 implemented in the FSL function *fslmaths.* DTI was estimated using FSL tool *dtifit* and excluded b=2000 shell from the fit. Employing the multi-shell data, DKI and WMTI metrics were estimated using Matlab code (https://github.com/NYU-DiffusionMRI/DESIGNER), (Fieremans et al., 2011)). NODDI metrics were derived using the AMICO algorithm implemented in Matlab

(https://github.com/daducci/AMICO). SMT mc metrics were estimated with the original code from Kaden and colleagues (https://github.com/ekaden/smt). RSI metrics were estimated using Matlab tools in-house.

In accordance with the first main aim of the study, we selected 21 scalar metrics from the six models (DTI, DKI, NODDI, RSI, SMT mc, WMTI) based on recent studies (Benitez et al., 2018; De Santis et al., 2011; Hope et al., 2019; Jelescu et al., 2015; Kaden, Kelm, et al., 2016; Maximov et al., 2019; Pines et al., 2020). Models were also selected based on what was within the frame of 'standard' diffusion models that could be used with our specific protocol and included available open source scripts. Figure 2 shows each of the included metrics for one participant, for illustrative purposes. All metrics and their corresponding abbreviations are summarised in the Supplementary material (SI table 1). In accordance with the second main aim of the study (iii), brain age prediction was performed for each model, using all available metrics extracted from a range of regions-of-interest (see section 2.5).

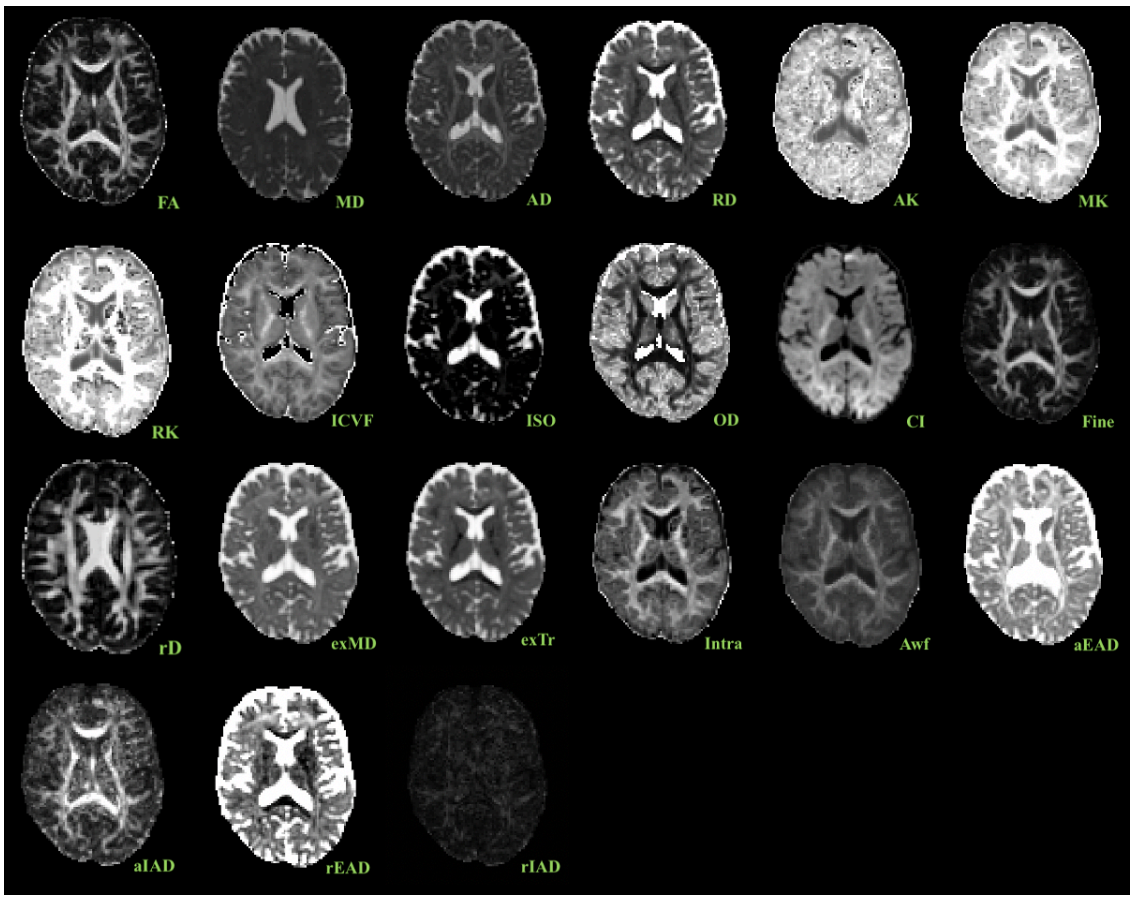

Figure 2. Diffusion metrics illustrated using one subject from the sample. **DTI**: *FA* (Fractional anisotropy), *MD* (Mean diffusivity), *AD* (Axial diffusivity), *RD* (Radial diffusivity). **DKI**: *AK* (Axial kurtosis), *MK* (Mean kurtosis), *RK* (Radial kurtosis). **NODDI**: *ICVF* (Intracellular volume fraction), *ISOVF* (Isotropic volume fraction), *OD* (Oriental dispersion). **RSI**: *CI* (cellular index), *Fine* (FA fine scale/slow compartment), *rD* (Restricted diffusivity coefficient). **SMT mc**: *exMD* (Extra cellular space), *exTr* (Extra-cellular space transverse), *Intra* (Intra axonal diffusivity). **WMTI**: *Awf* (Axonal water fraction), *aEAD, aIAD* (Axial extra and intra axonal diffusivity), *rEAD, rIAD* (Radial extra and intra axonal diffusivity).

2.4. Quality checking procedure

Prior to statistical analyses, a rigorous QC procedure was implemented to ensure data quality was optimal and not contaminated by motion, noise, or artefacts. Using a published approach (Roalf et al., 2016), we derived various quality assurance (QA) metrics (see Supplementary material; SI table 2), including temporal-signal-to-noise-ratio (TSNR). Detected outliers were manually checked and subsequently removed if deemed to have unsatisfactory data quality. A total of 52 datasets were removed, leaving the dataset at n = 702 scans. This dataset was put through the same inspection of metrics to ensure that quality assurance procedures were rigorous. As an additional step, images were also manually inspected if TSNR Z scores deviated minus or plus 2.5 standard deviations from the mean. Following this step, the final dataset remained at 702 scans from 573 individuals.

2.5. Tract-Based-Spatial-Statistics

Voxelwise statistical analysis of the FA data was carried out using Tract-Based Spatial Statistics (TBSS) (S. M. Smith et al., 2006), as part of FSL (S. M. Smith et al., 2004). First, FA images were brain-extracted using BET (S. M. Smith, 2002) and aligned into a common space (FMRI58_FA template) using the nonlinear registration tool FNIRT (Andersson, Jenkinson, & Smith., 2007; Jenkinson et al., 2012), which uses a b-spline representation of the registration warp field (Rueckert et al., 1999). Next, the mean FA image of all subjects was created and thinned to create a mean FA skeleton that represents the centres of all tracts common to the group. Each subject's aligned FA data was then projected onto this skeleton. The mean FA skeleton was thresholded at FA > 0.2. This procedure was repeated for all metrics. *fslmeants* was used to extract the mean skeleton and 20 regions of interest (ROI) based on a probabilistic white matter atlas (JHU) (Hua et al., 2008) for each metric. Including the mean skeleton values, 819 features per individual were derived (39 metrics x 20+1 ROIs). Of these, 21 metrics were used for age curve trajectories, linear mixed effect model analysis, and Wilk's theorem analysis, while all 819 MRI features were used for brain age analysis. Number of MRI features (corresponding to the sum of metric features) can be found in Table 4. Additional voxelwise analysis were carried out on the 573 subjects (excluding longitudinal measures) using the FSL tool Randomise, which performs permutation-based statistics (Winkler et al., 2014). 5000 permutations were run, where each diffusion metric was tested for its association with age using a threshold-free cluster enhancement method (TFCE; (S. Smith & Nichols, 2009)), thresholded at 0.975 to meet the equivalent $p < .05$ threshold for a one tailed test in each run, and corrected for multiple comparison. TBSS fill was used to create voxelwise statistical maps for each metric, which can be found in SI Figure 10.

2.6. Diffusion metric reproducibility

The validity and sensitivity of the different diffusion models essentially rely on the richness, quality and specific properties of the data used for model fitting. In order to assess the reproducibility of the included metrics (Maximov et al., 2015), we estimated the dMRI models using data obtained from different acquisition schemes varying the number of directions and maximum *b* value in 23 healthy subjects with mean age 35.77 years (SD = 8.37, 56.5% women). This represented a sub-sample of the full sample used in the current study. The following three acquisition schemes were compared: i) b=[1000,2000] with [60,30] directions, which is identical to the acquisition scheme used in the main analysis, ii) b=[1000,2000] with [60,60] directions and iii) b=[1000,2000,3000] with [60,60,60] directions. For each scheme we processed the data using an identical pipeline (Maximov et al., 2019) as described above and extracted the mean skeleton values for each of the included metrics. The main comparisons were performed using means of simple Pearson's correlation coefficients (see SI Figures 4, 5, and 6).

2.7. Statistical analysis

All statistical analyses were carried out using the statistical environment R, version 3.6.0 (www.r-project.org/) (R Core Team, 2012) and Python 3.7.0 (www.python.org/).

2.8. Linear mixed effects models (lme)

To investigate the relationship between age and global mean skeleton values for each diffusion metric, lme analyses were performed using the *lme* function (Bates & Pinheiro, 1998) in R (R Core Team, 2012). In fitting the model, we scaled (z normalised) each variable and entered age, orthogonalised polynomial age^2, sex, and timepoint (TP) as fixed effects. Subject ID was entered as a random effect. For each diffusion metric M, we employed the following function:

$$M = A + B \times Age + C \times Age^2 + Sex + TP \qquad (1)$$

where A is the intercept, B is the age coefficient, and C is the coefficient of the orthogonalised polynomial quadratic age term (expressed as *poly(age,2)[,2]* in R). Age curves were obtained with predictions from the fitted model using the *predict* function in R. Visual inspection of residual plots did not reveal any obvious deviations from homoscedasticity or normality. The significance threshold was set at $p < 0.05$, and the results were corrected for multiple comparisons using the false discovery rate (FDR) adjustment (Benjamini & Hochberg, 1995).

To investigate the rate of change for each of the age curves at any point, we calculated their derivatives using numerical differentiation with finite differences (Burden & Faires, 2011). To compare the age-sensitivity of the models, we ran lme fits with and without age terms, and calculated the difference in likelihood ratios (Glover & Dixon, 2004). The significance of the age dependence was calculated using Wilk's theorem (Wilks, 1938) as $\sqrt{2(L_2 - L_1)}$, where L_2 is the likelihood ratio obtained from the models with age terms, and L_1 is the likelihood ratio obtained from the models without age terms.

2.9. Brain-age prediction

The XGBoost regressor model was used to run the brain age prediction (https://xgboost.readthedocs.io/en/latest/python/index.html), including a decision-tree-based ensemble algorithm that has been used in recent large-scale brain age studies (A.-M. G. de Lange et al., 2019; Kaufmann et al., 2019). Parameters were set to max depth = 3, number of estimators = 100, and learning rate = 0.1 (defaults). For each diffusion model (DTI, DKI, NODDI, RSI, SMT mc, WMTI), predicted age was estimated in a 10-fold cross validation, assigning a model-specific brain age estimate to each individual, as well as a multimodal brain age estimate based on all diffusion features. To investigate the prediction accuracy of each model, correlation analyses were run for predicted versus chronological age, and model-specific R^2, root mean square error (RMSE) and mean absolute error (MAE) were calculated. To statistically compare the prediction accuracy of the models, Z tests for correlated samples (Zimmerman, 2012) were run on the model-specific correlations between predicted and chronological age in a pairwise manner using

$$Z = (\beta_{\mathrm{m1}} - \beta_{\mathrm{m2}}\}/\sqrt{\sigma_{\mathrm{m1}}^2 + \sigma_{\mathrm{m2}}^2 - 2\rho\sigma_{\mathrm{m1}}\sigma_{\mathrm{m2}}}$$

where “m1” and “m2” represent model 1 and model 2, the β terms represent the beta value from the regression fit, the σ terms represent their errors, and ρ represents the correlation between the two sets of associations. In order to assess the complementary value of the different models, we computed the correlations between the brain age predictions (Figure 6). The predictions were first corrected for age-bias using linear models (Le et al., 2018), and the residuals were used in the correlation analysis.

To evaluate the importance of each diffusion modality in the multimodal model, we ran an additional prediction model including only mean-skeleton values to reduce the number of highly correlated features in the regressor input, and calculated a) the proportion of the total

weight contributed by each modality, where weight represents the number of times a feature is used to split the data across all trees, and b) *gain* values, which represent the improvement in accuracy added by a feature to the branches it is on. To assess the significance of the general model performance, average RMSE was calculated for the multimodal model using cross validation with ten splits and ten repetitions and compared to a null distribution calculated from 1000 permutations.

3. Results

3.1. Diffusion metric reproducibility

The reproducibility of the estimated diffusion metrics based on data obtained with different acquisition schemes (described in 2.6) revealed overall high correlations between the mean skeleton values for all the model metrics. Highest overall reproducibility was observed for NODDI OD ($r(22) = 0.97$, $p < 0.001$) and RSI rD ($r(22) = 0.96$, $p < 0.001$). The lowest reproducibility was observed for WMTI radEAD ($r(22) = 0.44$, $p = 0.597$). Supplementary Table 4 and Supplementary Figures 4, 5, 6, and 7 show the results from the comparisons.

3.2. Age trajectories

Figure 3 shows the linear mixed effect model-derived age curves for each diffusion metric plotted as a function of age, where age curves are fitted with the predicted values of the lme models. Figure 4 shows all lme model-derived age curves from Figure 3 in standardised form in one plot. Figure 5 shows the derivatives of the lme fits, providing the estimated rate of change at every point (of age), including the point of change in trajectory for each model curve and the steepness of the turning point. Correlations between the metrics are available in the supplementary material (SI Figures 2 and 3) for both raw and standardised values respectively.

3.3. Comparing age curves

FA decreased steadily after the age of 30, with a steeper decline after the age of 50. MD, AD, and RD followed a reverse profile, with decreases in diffusivity until the 40's, whereby the trajectories subsequently increased thereafter. DKI metrics revealed patterns that closer resemble curvilinear trajectories, with NODDI ICVF, RSI CI, SMT mc intra, and WMTI awf metrics following similar trajectories. RSI rD, NODDI ISOFV, RSI FA fine, and WMTI axIAD metrics followed decreasing trajectories from the offset. SMT mc extramd and extratrans, and WMTI radEAD followed similar trajectories to MD and RD. NODDI OD revealed a steady increase until older age where the slope stabilised thereafter. Lastly, WMTI axEAD and radIAD showed u-trajectories (Figure 3).

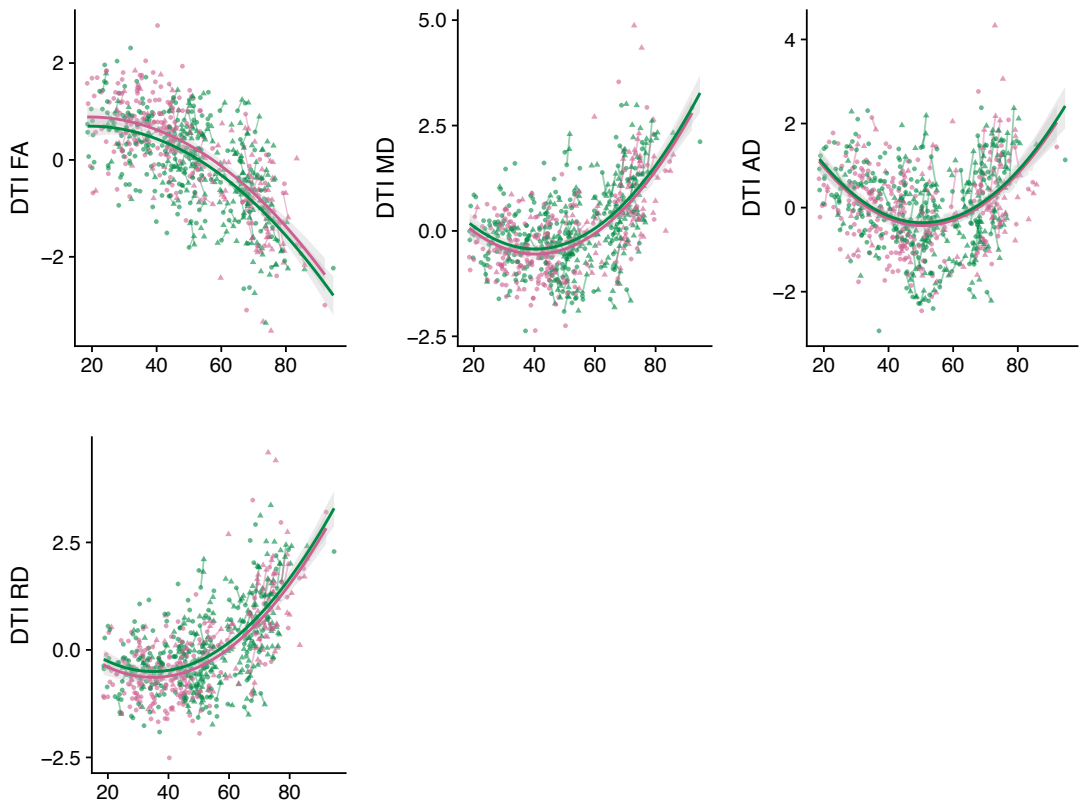
DTI FA
DTI MD
DTI AD
DTI RD
20
40
60
80

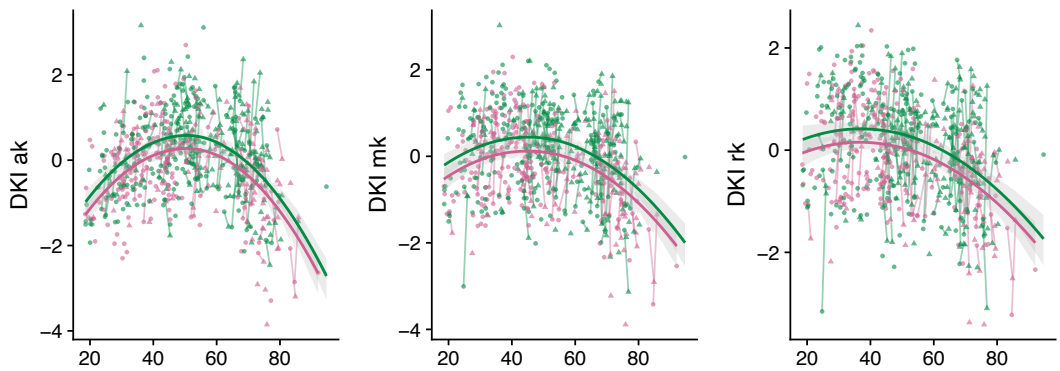
DKI ak
DKI mk
DKI rk
20
40
60
80

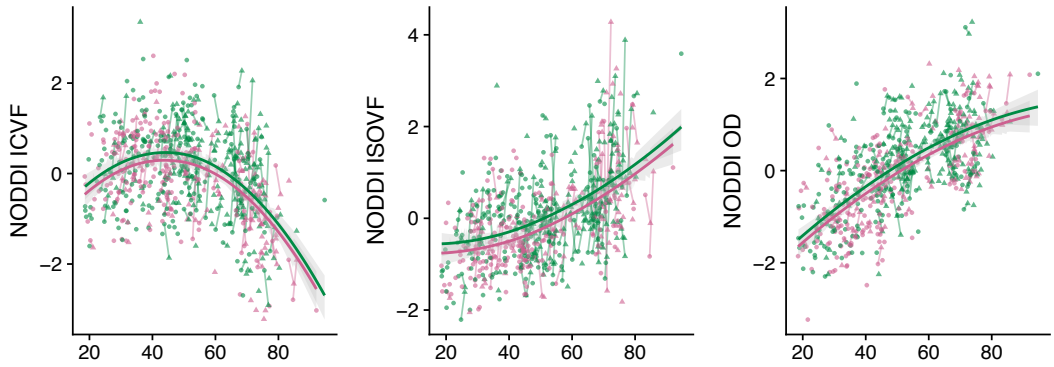
NODDI ICVF
NODDI ISOVF
NODDI OD
20
40
60
80

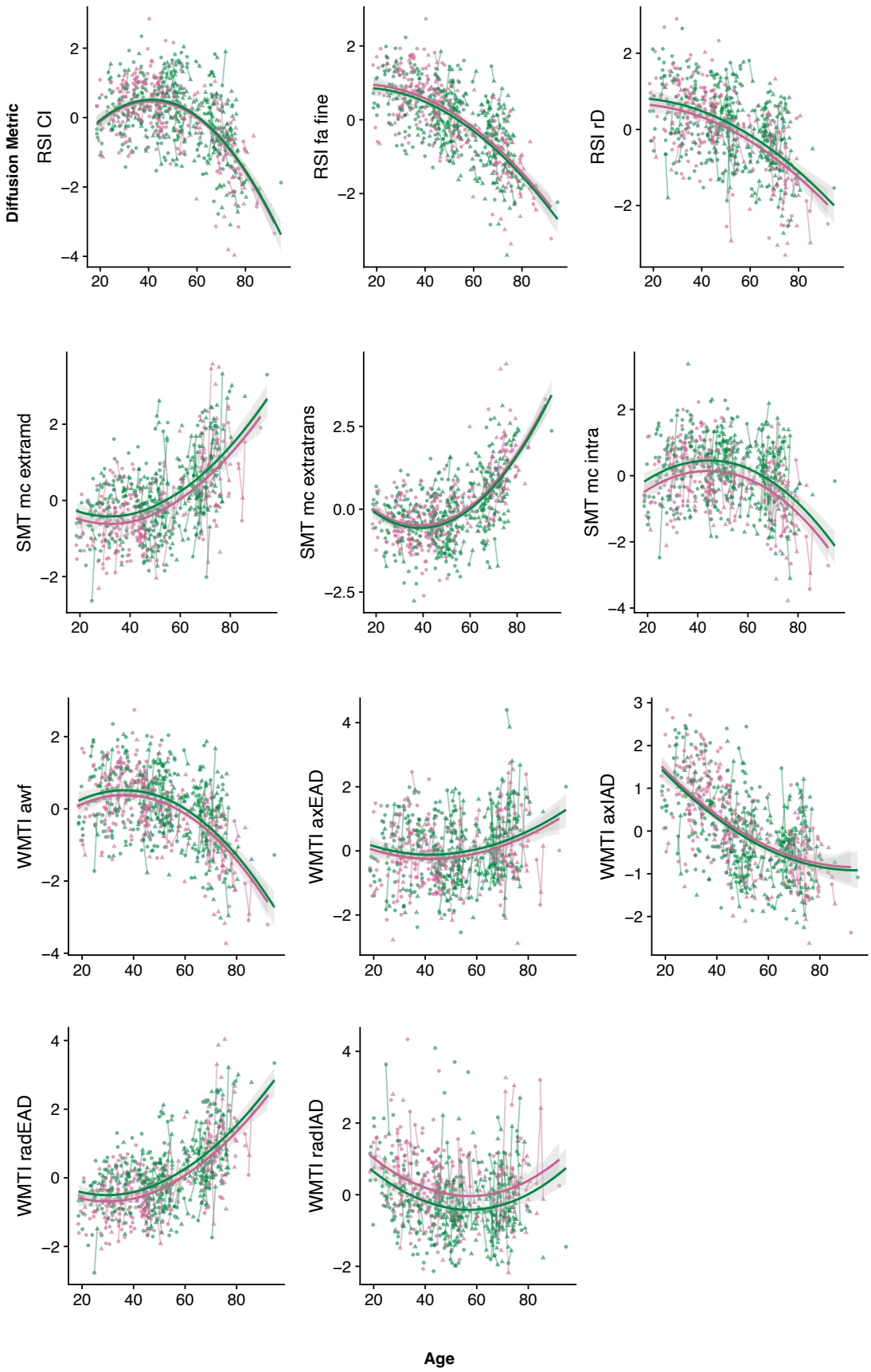

Figure 3. Age curves where each diffusion metric's standardised (z-score) mean skeleton value (y-axis) is plotted as a function of age (x-axis). Fitted lines made with lme-derived predicted values. Shaded areas represent 95% CI. Points connected by lines represent longitudinal data where circle is TP1 and triangle is TP2. Male subjects are represented by pink and female subjects by green.

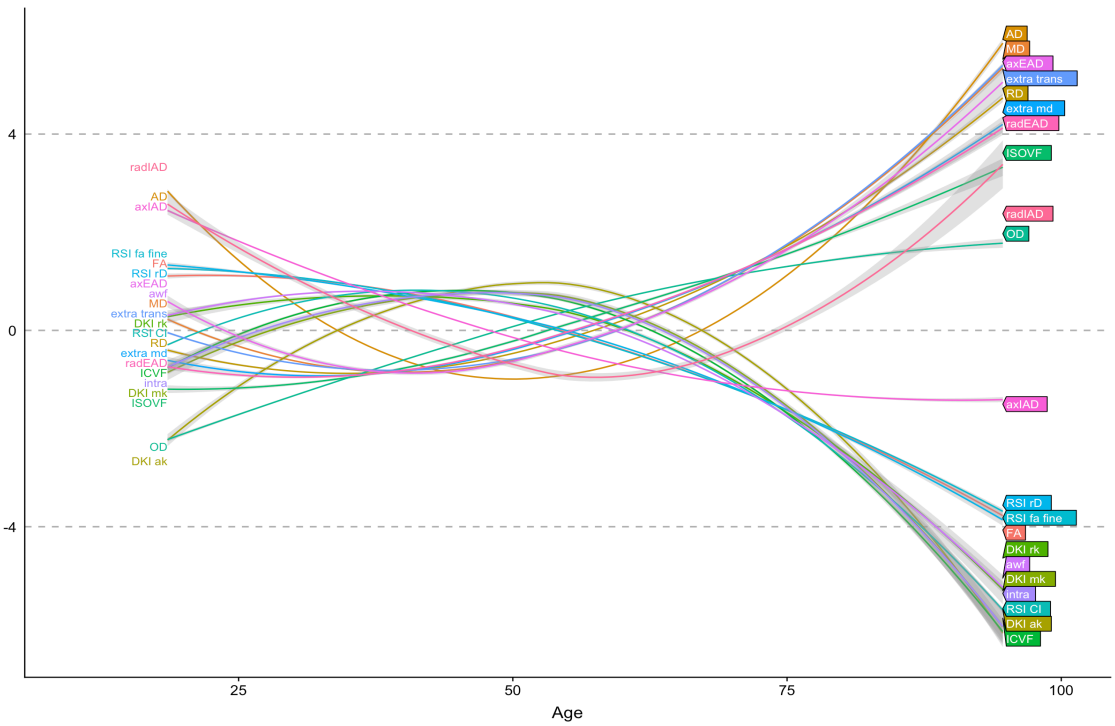

Figure 4. Plot displaying all lme-model derived age curves from Figure 3 in standardised form.

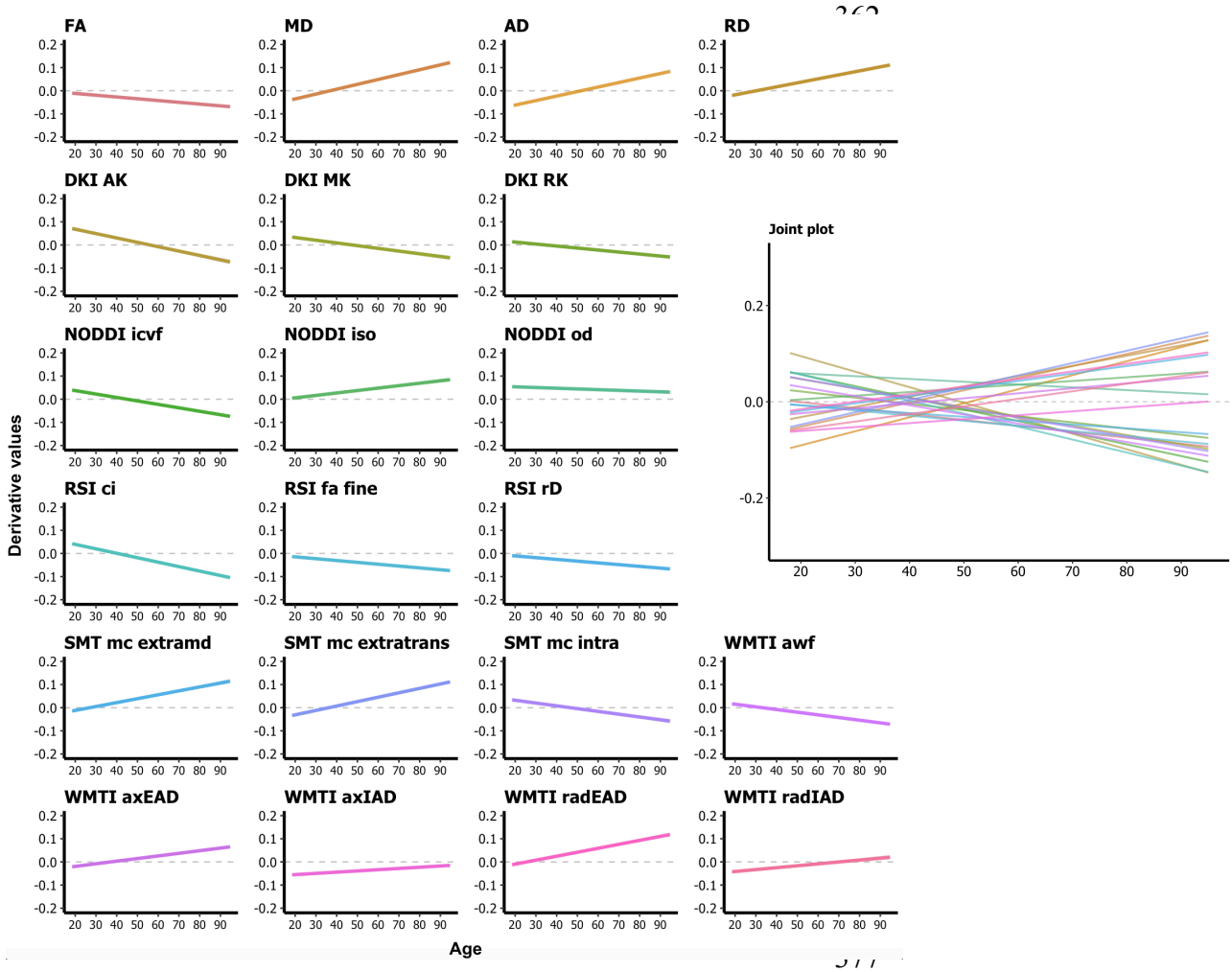

Figure 5. The derivative for each diffusion model, providing the estimated rate of change at every point. The point on the x-axis where the fitted line crosses 0 on the y-axis represents the turning point of the age trajectory for each metric.

Table 2. Linear mixed effect model results for each metric, where variables are *displayed with corresponding fixed effect estimates (β), (standard error), t-statistic, and FDR corrected P value.*

	FA	MD	AD	RD	DKI ak	DKI mk	DKI rk	NODDI icvf	NODDI isovf	NODDI OD	RSI CI	RSI fa fine	RSI rD	SMT mc extramd	SMT mc extratrans	SMT mc intra	WMTI awf	WMTI axEAD	WMTI axIAD	WMTI radEAD	WMTI radIAD
Age	-0.66***	0.46***	0.03	0.59***	-0.12*	-0.24***	-0.32***	-0.33***	0.48***	0.67***	-0.48***	-0.69***	-0.54***	0.50***	0.56***	-0.26***	-0.49***	0.15***	-0.58***	0.57***	-0.12*
	(0.03)	(0.04)	(0.04)	(0.03)	(0.04)	(0.04)	(0.04)	(0.04)	(0.04)	(0.03)	(0.04)	(0.03)	(0.04)	(0.04)	(0.03)	(0.04)	(0.04)	(0.04)	(0.04)	(0.03)	(0.04)
	-20.76	13.19	0.71	18.02	-3.21	-5.95	-8.09	-8.52	13.31	21.62	13.79	-21.97	-14.89	14.31	16.66	-6.68	-13.33	3.51	-16.43	17.11	-2.92
	5.21 x 10^{-41}	4.12 x 10^{-24}	1	3.09 x 10^{-35}	0.02	2.69 x 10^{-07}	9.61 x 10^{-12}	4.50 x 10^{-13}	2.12 x 10^{-24}	9.62 x 10^{-43}	1.51 x 10^{-25}	1.97 x 10^{-43}	3.78 x 10^{-28}	8.84 x 10^{-27}	3.26 x 10^{-32}	7.50 x 10^{-09}	1.96 x 10^{-24}	6.46 x 10^{-03}	1.07 x 10^{-31}	3.12 x 10^{-33}	0.03
Age^2	-0.17***	0.34***	0.40***	0.29***	-0.44***	-0.26***	-0.18***	-0.33***	0.10*	-0.08	-0.37***	-0.15***	-0.11*	0.21***	0.35***	-0.27***	-0.26***	0.14***	0.11*	0.21***	0.21***
	(0.03)	(0.03)	(0.04)	(0.03)	(0.04)	(0.04)	(0.04)	(0.04)	(0.03)	(0.03)	(0.03)	(0.03)	(0.03)	(0.03)	(0.03)	(0.04)	(0.03)	(0.04)	(0.03)	(0.03)	(0.04)
	-5.57	10.30	10.63	9.37	-12.34	-7.15	-4.77	-9.04	3.11	-2.66	-11.04	-4.93	-3.16	6.46	10.99	-7.42	-7.51	3.63	3.36	6.91	5.76
	1.56 x 10^{-06}	2.34 x 10^{-17}	7.18 x 10^{-18}	4.20 x 10^{-15}	4.69 x 10^{-22}	1.32 x 10^{-09}	5.25 x 10^{-05}	5.25 x 10^{-14}	0.02	0.09	3.64 x 10^{-19}	2.73 x 10^{-05}	0.02	2.26 x 10^{-08}	4.82 x 10^{-19}	3.28 x 10^{-10}	1.04 x 10^{-10}	6.46 x 10^{-03}	0.01	2.28 x 10^{-09}	1.29 x 10^{-06}
Sex	-0.09**	0.06	0.03	0.07*	0.14***	0.16***	0.13***	0.08	0.10*	0.07	0.02	-0.05	0.08	0.10*	-0.03	0.15***	0.07	0.06	-0.03	0.09*	-0.19***
	(0.03)	(0.03)	(0.04)	(0.03)	(0.04)	(0.04)	(0.04)	(0.04)	(0.03)	(0.03)	(0.03)	(0.03)	(0.03)	(0.03)	(0.03)	(0.04)	(0.03)	(0.04)	(0.03)	(0.03)	(0.04)
	-3.12	1.75	0.78	2.16	4.00	4.19	3.48	2.20	2.90	2.48	0.62	-1.55	2.24	2.90	-1.07	4.10	1.88	1.56	-1.00	2.86	-4.96
	1.59 x 10^{-02}	0.58	1	0.23	1.10 x 10^{-03}	3.72 x 10^{-04}	4.76 x 10^{-03}	0.21	0.03	0.10	1	0.86	0.19	0.03	1	5.16 x 10^{-04}	0.44	0.85	1	0.03	2.40 x 10^{-05}
Timepoint	0.01	0.02	0.03	0.01	0.07	0.04	0.02	0.04	0.05	0.02	0.03	0.001	-0.01	0.06	-0.02	0.04	0.03	0.03	-0.02	0.05	-0.05
	(0.01)	(0.01)	(0.02)	(0.01)	(0.03)	(0.03)	(0.03)	(0.03)	(0.03)	(0.01)	(0.01)	(0.01)	(0.02)	(0.03)	(0.01)	(0.03)	(0.02)	(0.03)	(0.02)	(0.02)	(0.04)
	0.88	1.55	1.72	1.02	2.36	1.21	0.64	1.62	1.64	1.33	1.95	0.05	-0.30	2.31	-1.44	1.32	1.41	1.03	-0.66	2.19	-1.30
	1	0.65	0.93	1	0.10	1	1	0.57	0.54	0.98	0.37	1	1	0.12	1	1	0.84	1	1	0.16	1
Observations	702	702	702	702	702	702	702	702	702	702	702	702	702	702	702	702	702	702	702	702	702
Log Likelihood	-651.72	-741.08	-853.38	-671.25	-885.78	-941.80	-945.41	-885.92	-882.34	-678.79	-748.66	-662.96	-829.12	-832.39	-703.69	-932.36	-849.65	-965.60	-816.35	-795.04	-956.32
Akaike Inf. Crit.	1,317.44	1,496.15	1,720.76	1,356.50	1,785.56	1,897.60	1,904.81	1,785.84	1,778.69	1,371.58	1,511.33	1,339.91	1,672.24	1,678.79	1,421.39	1,878.73	1,713.30	1,945.20	1,646.69	1,604.09	1,926.65
Bayesian Inf. Crit.	1,349.27	1,527.98	1,752.59	1,388.33	1,817.39	1,929.43	1,936.64	1,817.67	1,810.52	1,403.40	1,543.15	1,371.74	1,704.06	1,710.62	1,453.21	1,910.55	1,745.13	1,977.02	1,678.52	1,635.92	1,958.48

Note: Age^2 represents the orthogonalised polynomial quadratic age term (Eq. 1)

$^{*}p<0.05$; $^{**}p<0.01$; $^{***}p<0.001$

3.4. Age sensitivity estimated using lme models

Results from the lme models revealed significant main effects of age on the global mean skeleton values for all diffusion metrics (see Table 2). An examination of the fixed effects estimates (β) and t-statistics for the age term allows for interpretation of the extent and direction of the linear association with age. Overall, the FA fine compartment of the RSI model was most sensitive to age ($\beta(125) = -0.69$, $t = -21.97$, $p < 0.001$). NODDI OD was the second most sensitive to age ($\beta(125) = 0.67$, $t = 21.62$, $p < 0.001$). The model least sensitive to age was DTI AD ($\beta(125) = 0.03$, $t = 0.71$, $p = 0.48$). For conventional DTI metrics, FA was the most age sensitive ($\beta(125) = -0.66$, $t = -20.76$, $p < 0.001$). No main effects of timepoint survived correction for multiple comparisons.

3.5. Age sensitivity estimated using Wilk's theorem

Table 3 shows the strength of the overall age variation for each metric estimated by the difference in likelihood values (described in Section 2.8). All metrics showed significant age dependence, with RSI FA fine as the most age sensitive (z = 18.79), followed by NODDI OD (z = 18.55) and DTI-based FA (z = 18.12). WMTI radIAD (z = 5.61) was the least age-dependant metric.

Table 3 Likelihood values from the lme models without age terms (L_1) and with age terms (L_2). The significance of the age dependence is estimated by the difference in likelihood values using Wilk's theorem. FDR corrected p-values = p^{corr}.

Model		L_1	L_2	Difference (z)	*p-value*	p^{corr}
DTI	FA	-815.86	-651.72	18.12	5.22×10^{-72}	1.10×10^{-70}
	MD	-848.36	-741.08	14.65	2.55×10^{-47}	5.35×10^{-46}
	AD	-900.66	-853.38	9.72	2.93×10^{-21}	6.15×10^{-20}
	RD	-820.44	-671.25	17.27	1.62×10^{-65}	3.40×10^{-64}
DKI	AK	-952.44	-885.78	11.55	1.12×10^{-29}	2.36×10^{-28}
	MK	-977.09	-941.80	8.40	4.71×10^{-16}	9.89×10^{-15}
	RK	-981.65	-945.41	8.51	1.83×10^{-16}	3.83×10^{-15}
NODDI	ICVF	-948.54	-885.92	11.19	6.40×10^{-28}	1.34×10^{-26}
	ISOVF	-957.61	-882.34	12.27	2.06×10^{-33}	4.33×10^{-32}
	OD	-850.84	-678.79	18.55	1.90×10^{-75}	3.99×10^{-74}
RSI	CI	-866.73	-748.66	15.37	5.28×10^{-52}	1.11×10^{-50}
	FA fine	-839.53	-662.96	18.79	2.07×10^{-77}	4.36×10^{-76}
	rD	-922.24	-829.12	13.65	3.62×10^{-41}	7.60×10^{-40}
SMT mc	Extra md	-929.01	-832.39	13.90	1.10×10^{-42}	2.31×10^{-41}
	Extra trans	-848.79	-703.69	17.03	9.71×10^{-64}	2.04×10^{-62}
	Intra	-973.21	-932.36	9.04	1.82×10^{-18}	3.82×10^{-17}
WMTI	AWF	-942.66	-846.37	13.88	1.52×10^{-43}	3.19×10^{-41}
	axEAD	-973.15	-962.32	4.65	1.98×10^{-05}	4.17×10^{-04}
	axIAD	-930.26	-816.35	15.09	3.38×10^{-50}	7.10×10^{-49}
	radEAD	-922.92	-795.04	15.99	2.91×10^{-56}	6.10×10^{-55}
	radIAD	-972.08	-955.32	5.61	1.43×10^{-07}	3.00×10^{-06}

3.6. Age sensitivity estimated using brain age

The model performances for the multimodal and model-specific brain age predictions are shown in Table 4. SI Figures 8 and 9 show the associations between predicted age and chronological age for each of the models. Figure 6 shows the correlations between predicted brain age for each model, indicating the amount of shared variance explained by the models. Pairwise differences in the age prediction accuracy of the models are shown in Figures 7 and 8. SI Figure 1 shows the RMSE of the multimodal model prediction compared to a null distribution.

Table 4. Number of MRI variables (corresponding to the sum of metric features), root mean square error (RMSE), mean absolute error (MAE), correlation between predicted and chronological age (Pearson's r), and R^2 for each of the models. CI = confidence interval.

Model	MRI variables	RMSE	MAE	r [95% CI]	R^2 [95% CI]
DTI	105	8.88	7.00	0.85 [0.82, 0.86]	0.71 [0.69, 0.74]
DKI	63	12.19	9.82	0.68 [0.64, 0.72]	0.46 [0.41,0.52]
NODDI	63	9.15	7.31	0.83 [0.81, 0.86]	0.70 [0.65, 0.74]
RSI	252	8.93	7.13	0.84 [0.82, 0.86]	0.71 [0.69,0.74]
SMT mc	231	10.70	8.41	0.76 [0.73, 0.79]	0.58 [0.54, 0.62]
WMTI	105	9.40	7.41	0.82 [0.80, 0.85]	0.68 [0.64, 0.72]
Multimodal	819	8.26	6.52	0.87 [0.85, 0.88]	0.75 [0.73, 0.77]

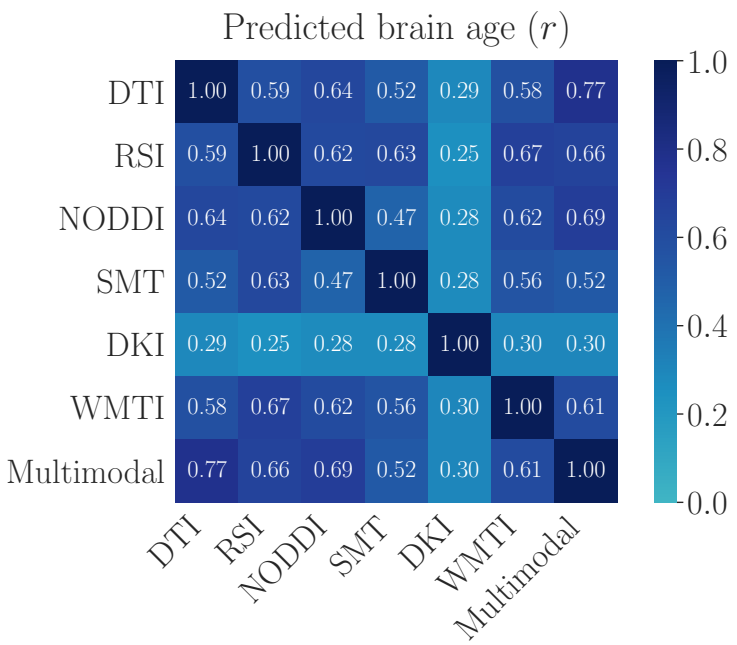

Figure 6. Correlation matrix for predicted brain age of each modality and the multimodal model, indicating the amount of shared variance explained by the models. The prediction values were first corrected for chronological age using linear models, and the residuals were used in the correlation analysis.

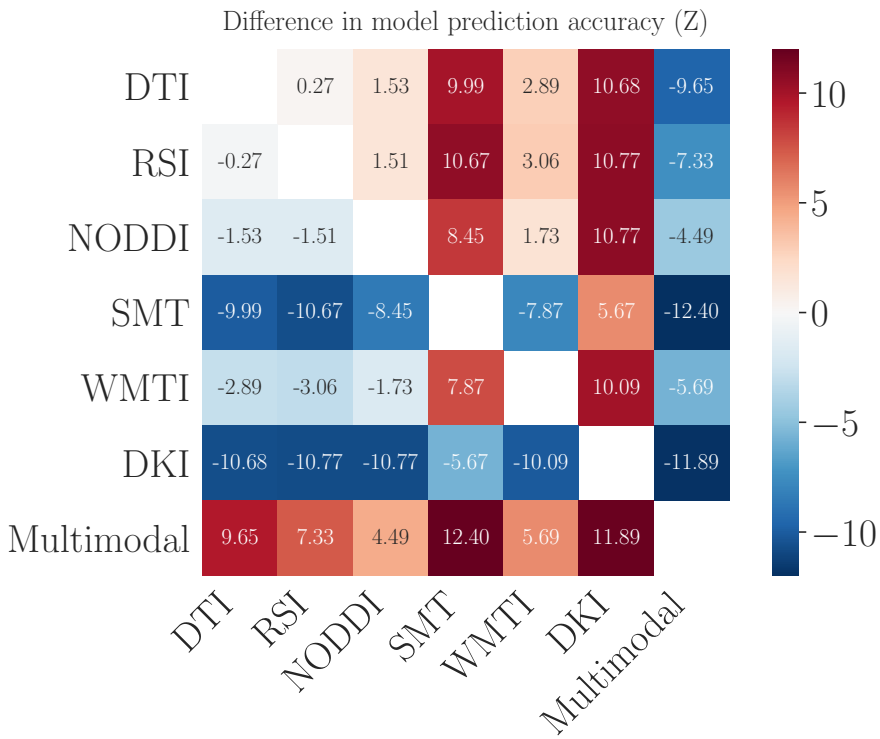

Figure 7. Matrix showing pairwise differences between the model prediction accuracies (correlations between predicted and chronological age), based on z tests for correlated samples.

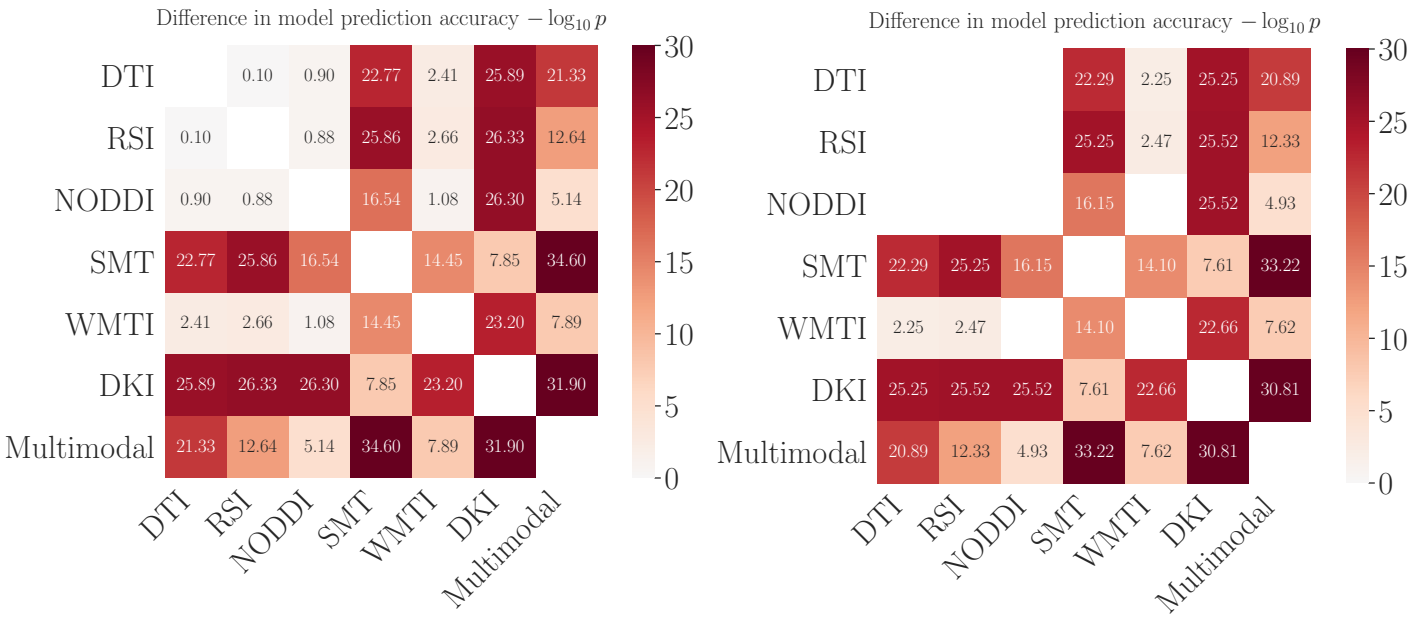

Figure 8. Log10(p) values of the pairwise differences between the model prediction accuracies. Higher numbers represent more significant differences. Left: uncorrected p-values. Right: P-values corrected for multiple comparisons using FDR, with non-significant (> 0.05) values masked out.

As visible from Table 4, the multimodal model showed the most accurate age prediction (r = 0.87, $p < 0.001$, 95% CI = [0.85, 0.88]), while the DKI model performed the worst (r = 0.68, $p < 0.001$, 95% CI = [0.64, 0.72]). As shown in Figures 7 and 8, the multimodal prediction accuracy was significantly higher than the accuracy of each of the other models, with the largest difference seen between the multimodal model and DKI. The differences in prediction accuracy between DTI and RSI, and WMTI and NODDI did not survive correction for multiple comparisons. Figure 6 showed correlation coefficients of mean r = 0.57 (Std = 0.12) between the DTI, RSI, NODDI, SMT and WMTI predictions, while the DKI showed lower correlations with the other model predictions (mean r = 0.28, Std = 0.02).

To evaluate the relative importance of each modality, we ran an additional multimodal model including only mean-skeleton values to reduce the number of highly correlated features in the regressor input. Table 5 shows the total gain and the proportion of weight contributed by each modality to the total weight, indicating their relative contribution in the model training. The results revealed that the machine favoured the DTI model in the training.

Table 5. Feature importance evaluated using a reduced multimodal model that included only mean skeleton values for each modality. Number of MRI variables (corresponding to the sum of metric features), percentage contribution to the total weight, and total gain for each modality.

Model	MRI variables	% of total weight	Total gain
DTI	5	55.99	470299.745
DKI	3	3.25	27309.38
NODDI	3	13.70	115067.81
RSI	11	15.53	130445.88
SMT mc	10	6.93	58184.65
WMTI	5	4.60	38651.378

4. Discussion

Ageing confers a range of structural brain alterations, affecting micro- and macrostructural properties of the neurocircuitry supporting cognitive and other complex brain functions. In the current mixed cross-sectional and longitudinal study, we compared advanced and conventional dMRI models in their ability to investigate brain white matter age trajectories across the adult lifespan, with specific interest in understanding the how and to what extent each model is sensitive to the process of ageing. In summary, the results from our comprehensive analysis approach, including age-curve trajectories, linear mixed effects models, Wilk's theorem analysis, and brain age prediction, showed high age sensitivity for all diffusion metrics, with comparable sensitivity between the highest performing advanced dMRI models and

481 conventional DTI. The mixed effects analyses and corresponding derivatives revealed
482 variations in age trajectories between models, indicating that they may pick up different
483 underlying aspects of white matter ageing. Our brain age prediction analysis using advanced
484 dMRI models of RSI and NODDI are the first of any study to utilise these models for brain age
485 prediction accuracy.

486 Our results showed that increasing white matter trajectories of FA plateaued around the
487 third decade with a steady decline in slope following the age of ~40, and an accelerated
488 decrease in senescence (Figure 3). The other DTI metrics of MD, AD, and RD revealed
489 decreases in diffusivity up until the 40-50-year age mark, where the trajectories subsequently
490 increase following a steady period. While these results to a large extent correspond with
491 trajectories observed in previous studies (Cox et al., 2016; Davis et al., 2009; Westlye et al.,
492 2010), a more defined inverted U-shape (Westlye et al., 2010) was less prominent in our study,
493 likely due to a lack of younger participants below the age of 20.

494 While several of the dMRI models including conventional DTI showed comparable
495 results in terms of age sensitivity, the inclusion of the advanced dMRI models offer new
496 insight, with visibly different age trajectories (Figure 3), including variation in turning points
497 (Figure 4) and gradient of change (Figure 5). Although diffusion imaging cannot give direct
498 access to neuronal processes on a cellular level, the findings could reflect that the dMRI
499 models show differential sensitivity to biological mechanisms involved in white matter ageing,
500 given that they are good approximations to the underlying white matter fibre organisation
501 (Jelescu & Budde, 2017). The variation in turning points and gradient of change calculated
502 using the derivates of each model informs us about the estimated rate of change at specific
503 ages, in addition to the differential sensitivity between different metrics during different life
504 phases. These metric-specific differences may reflect age-related pathological changes behind
505 each dMRI model. DTI measurements have already been dubbed as sensitive markers for
506 neuropathological changes observed in the brain (A. L. Alexander et al., 2008). While
507 speculative, utilising advanced dMRI models in addition to conventional DTI may provide
508 more specificity in the interpretation of the results and improve specificity of tissue pathology.
509 This, in turn, may lead to better understanding of the neuropathological basis for a range of
510 diseases associated with white matter architecture that deviates from that which is expected
511 with normal healthy ageing. Investigating multiple dMRI models in combination with
512 histological studies and animal research could also be valuable for comparison of fibre
513 architecture (Jbabdi & Johansen-Berg, 2011), which could help identifying tissue-specific
514 biomarkers of white matter ageing and disease.

While conventional DTI is limited by underestimation of diffusion restriction in voxels within crossing fibres (Pines et al., 2020) and lacks geometric specificity to allow for inference regarding tissue properties, advanced (tissue) models come with the potential to better characterise the underlying biology (Jelescu & Budde, 2017). If assumptions of underlying microstructure are valid, these advanced models represent a promising contribution to the investigation of brain development and ageing, and aberrant brain biology in various clinical conditions (D. C. Alexander et al., 2019). Interestingly, FA based on the relatively simple DTI model utilising only single-shell data offered one of the highest sensitivities to age, which was also supported by the brain age prediction analysis. While the metrics based on the RSI model yielded highly similar age sensitivity, the overall strong performance of the DTI metrics supports that DTI provides sensitive measures of gross white matter anatomy. However, it should be emphasised that DTI is a model of signal representation sensitive to the whole richness of the diffusion signal, while the tissue models are more susceptible to artefacts and noise due to the model assumptions relevant for characterising tissue geometry, which limit their ability to detect subtle changes in the diffusion signal. Additionally, metrics of biophysical models are biologically specific, which limits their sensitivity typically to one white matter feature, such as the axonal water fraction or the extra-axonal space, in contrast to FA which is sensitive to all of the diffusion signal estimated as one single compartment. As such, the DTI model's sensitivity to age does not necessarily imply biological relevance or specificity. Considering a range of complementary diffusion models may thus offer benefits in terms of biological interpretations and individualised predictions in clinical studies. Further studies including clinical samples are needed to pursue this hypothesis.

While considering a range of diffusion models, it is important to note that each comes with its respective limitations. NODDI has been particularly criticised in recent years, with research suggesting the model assumptions are invalid (Lampinen et al., 2017). NODDI provides estimates of geometric parameters only, with there being an absence of any direct diffusivity estimation (Jelescu et al., 2015). DKI, like DTI, is limited in specificity as it can be affected by different features of tissue microstructure. Thus, the biophysical model that relates DKI parameters directly to white matter microstructure (WMTI, (Fieremans et al., 2011)) was proposed. However, assumptions made in WMTI may be oversimplifying, which could lead to bias in the estimated parameters in addition to reduced information about the microstructure. WMTI parameter estimation accuracy is also said to progressively degrade with higher orientation dispersion (Jelescu et al., 2015). The SMT mc model overcomes limitations in WMTI (Fieremans et al., 2011) and NODDI (Zhang et al., 2012) as it makes no assumptions about the neurite orientation distribution (Kaden, Kelm, et al., 2016). However, it is limited by

assuming that the effective transverse diffusivity inside the neurites is zero, an approximation which may not hold for unmyelinated axons and dendrites (Kaden, Kelm, et al., 2016), due to possible neurite undulation on the microscopic scale (Nilsson et al., 2012). RSI, like most diffusion-based techniques, suffers from low resolution and may best be utilised in supplement to high spatial resolution sequences as part of a multimodal imaging protocol (Brunsing et al., 2017). For example, the DTI model's limitation of being blind to crossing and bending fibres may be resolved by the RSI models multi-direction properties and ability to measure diffusion orientation and length scale (White et al., 2013).

Despite the limitations of each model, and possible redundancy between them, assessing age-related white microstructural changes using a combination of diffusion models can be advantageous. Biophysical models of WMTI and SMT mc for example, adds the possibility for assessing the separate effect of diffusion in intra- and extra-axonal space (Jelescu & Budde, 2017; Voldsbekk et al., 2020). Some methodological limitations concern that of the TBSS approach, where we are only assessing the core of the major white matter pathways and are blind to more peripheral regions as well as grey matter. Additionally, averaging over the entire white matter skeleton is complicated by the direction of age associations varying regionally. As such, averaging over the entire white matter skeleton may counteract two opposing effects. Lastly, we used DTI (specifically FA) to generate white matter skeletons. Future research should consider generating white matter skeletons based on advanced diffusion maps that are more resistant to crossing fibres.

The current study also comes with several strengths. One strength concerns the direct tests of the reproducibility of the included dMRI metrics across different acquisition schemes with a higher number of directions and *b*-values, which supports the use of advanced computational dMRI models for data obtained using a clinically feasible acquisition protocol. Another strength of the current study is that it utilises a combination of advanced dMRI models based on multi-shell acquisition, which turn over more detailed features of the cellular environment from differential tissue responses elicited by the different *b*-values (Assaf & Basser, 2005; Clark et al., 2002; Pines et al., 2020). The study also included a relatively large sample size and benefitted from all participants having been scanned with the same MRI scanner. Additionally, with cross-sectional studies being limited by between-subject variance and possible cohort effects (Schaie, 2005), the current study profits from a mixed cross-sectional and longitudinal design, where subjects can be used as their own baseline (Sexton et al., 2014) and better inform us of the ageing process, as well as providing a better indication of estimates we can make about an individual's ageing trajectory. However, the longitudinal aspect of our study had some limitations, including the short interval duration, and the low

sample size compared to the cross-sectional sample. Consequently, the main results were largely driven by cross sectional data despite the mixed cross-sectional and longitudinal nature of the design. Future research should aim to adopt fully longitudinal designs over several time points in order to evaluate individual differences in change over time, preferably over wide age ranges.

Although the advanced dMRI models offered new insight into age sensitivity (such as the use of brain-age prediction accuracy of RSI and NODDI) and differences in age trajectories, the biological interpretation of these metrics remain vague (Hope et al., 2019). Continued development and validation of more optimal diffusion models that better reflect biological properties of the brain is needed, and future research should take into account the impact of a range of potential factors that may mediate brain and cognitive development (Alnæs et al., 2019) and ageing (Lindenberger, 2014), such as pre- and perinatal events, socio-demographical factors, education, lifestyle, cardiometabolic risk factors, and genetics.

In conclusion, characterising changes in white matter microstructure over the human lifespan is critical for establishing robust baseline measures of normative development and ageing, which in turn can help us to better understand deviations from healthy age trajectories. The current study demonstrates that while advanced and conventional dMRI models show comparable age-sensitivity, multi-shell diffusion acquisition and advanced dMRI models can contribute to measuring multiple, complementary aspects of white matter changes across age. Further developing dMRI models in terms of biological tissue specificity remains a challenging yet important goal for understanding white matter development across the human lifespan.

Acknowledgements and funding

The study is supported by the Research Council of Norway (223273, 249795, 248238, 286838), the South-Eastern Norway Regional Health Authority (2014097, 2015044, 2015073, 2016083, 2018037, 2018076), the Norwegian ExtraFoundation for Health and Rehabilitation (2015/FO5146), KG Jebsen Stiftelsen, ERA-Net Cofund through the ERA PerMed project ‘IMPLEMENT’, and the European Research Council under the European Union's Horizon 2020 research and Innovation program (ERC StG, Grant 802998).

We wish to thank the following colleagues for their considerable effort in helping with the data collection: Aili Røtterud Løchen, Linn Sofie Sæther, Jennifer Monereo Sanchez, Lilly Susanne Lengali, Øyvind Rustan, and Martine Dæhlen.

5. References

Alexander, A. L., Lee, J. E., Lazar, M., & Field, A. S. (2008). *Diffusion Tensor Imaging of the Brain*. 26.

Alexander, D. C., Dyrby, T. B., Nilsson, M., & Zhang, H. (2019). Imaging brain microstructure with diffusion MRI: Practicality and applications. *NMR in Biomedicine*, *32*(4), e3841. https://doi.org/10.1002/nbm.3841

Alnæs, D., Kaufmann, T., Marquand, A. F., Smith, S. M., & Westlye, L. T. (2019). *Patterns of socio-cognitive stratification and perinatal risk in the child brain* [Preprint]. Neuroscience. https://doi.org/10.1101/839969

Andersson, J. L. R., & Sotiropoulos, S. N. (2015). Non-parametric representation and prediction of single- and multi-shell diffusion-weighted MRI data using Gaussian processes. *NeuroImage*, *122*, 166–176. https://doi.org/10.1016/j.neuroimage.2015.07.067

Andersson, J. L. R., & Sotiropoulos, S. N. (2016). An integrated approach to correction for off-resonance effects and subject movement in diffusion MR imaging. *NeuroImage*, *125*, 1063–1078. https://doi.org/10.1016/j.neuroimage.2015.10.019

Assaf, Y., & Basser, P. J. (2005). Composite hindered and restricted model of diffusion (CHARMED) MR imaging of the human brain. *NeuroImage*, *27*(1), 48–58. https://doi.org/10.1016/j.neuroimage.2005.03.042

Barrick, T. R., Charlton, R. A., Clark, C. A., & Markus, H. S. (2010). White matter structural decline in normal ageing: A prospective longitudinal study using tract-based spatial statistics. *NeuroImage*, *51*(2), 565–577. https://doi.org/10.1016/j.neuroimage.2010.02.033

Bates, D. M., & Pinheiro, J. C. (1998). LINEAR AND NONLINEAR MIXED-EFFECTS MODELS. *Conference on Applied Statistics in Agriculture*. https://doi.org/10.4148/2475-7772.1273

Bender, A. R., & Raz, N. (2015). Normal-appearing cerebral white matter in healthy adults: Mean change over 2 years and individual differences in change. *Neurobiology of Aging*, *36*(5), 1834–1848. https://doi.org/10.1016/j.neurobiolaging.2015.02.001

Bender, A. R., Völkle, M. C., & Raz, N. (2016). Differential aging of cerebral white matter in middle-aged and older adults: A seven-year follow-up. *NeuroImage*, *125*, 74–83. https://doi.org/10.1016/j.neuroimage.2015.10.030

Benitez, A., Jensen, J. H., Falangola, M. F., Nietert, P. J., & Helpern, J. A. (2018). Modeling white matter tract integrity in aging with diffusional kurtosis imaging. *Neurobiology of Aging*, *70*, 265–275. https://doi.org/10.1016/j.neurobiolaging.2018.07.006

Benjamini, Y., & Hochberg, Y. (1995). Controlling the False Discovery Rate: A Practical and Powerful Approach to Multiple Testing. *Journal of the Royal Statistical Society: Series B (Methodological)*, *57*(1), 289–300. https://doi.org/10.1111/j.2517-6161.1995.tb02031.x

Brunsing, R., Schenker-Ahmed, N. M., White, N. S., Parsons, J. K., Kane, C., Kuperman, J., Bartsch, H., Kader, A. K., Rakow-Penner, R., Seibert, T. M., Margolis, D., Raman, S. S., McDonald, C. R., Farid, N., Kesari, S., Hansel, D., Shabaik, A., Dale, A. M., & Karow, D. S. (2017). Restriction Spectrum Imaging: An evolving imaging biomarker in prostate magnetic resonance imaging. *Journal of Magnetic Resonance Imaging : JMRI*, *45*(2), 323–336. https://doi.org/10.1002/jmri.25419

Chung, S., Fieremans, E., Wang, X., Kucukboyaci, N. E., Morton, C. J., Babb, J., Amorapanth, P., Foo, F.-Y. A., Novikov, D. S., Flanagan, S. R., Rath, J. F., & Lui, Y. W. (2018). White Matter Tract Integrity: An Indicator of Axonal Pathology after Mild Traumatic Brain Injury. *Journal of Neurotrauma*, *35*(8), 1015–1020. https://doi.org/10.1089/neu.2017.5320

Clark, C. A., Hedehus, M., & Moseley, M. E. (2002). In vivo mapping of the fast and slow diffusion tensors in human brain. *Magnetic Resonance in Medicine*, *47*(4), 623–628. https://doi.org/10.1002/mrm.10118

Cole, J. H., Ritchie, S. J., Bastin, M. E., Hernández, M. C. V., Maniega, S. M., Royle, N., Corley, J., Pattie, A., Harris, S. E., Zhang, Q., Wray, N. R., Redmond, P., Marioni, R. E., Starr, J. M., Cox, S. R., Wardlaw, J. M., Sharp, D. J., & Deary, I. J. (2018). Brain age predicts mortality. *Molecular Psychiatry*, *23*(5), 1385–1392. https://doi.org/10.1038/mp.2017.62

Cole, James H. (2019). *Multi-modality neuroimaging brain-age in UK Biobank: Relationship to biomedical, lifestyle and cognitive factors* [Preprint]. Neuroscience. https://doi.org/10.1101/812982

Cox, S. R., Ritchie, S. J., Tucker-Drob, E. M., Liewald, D. C., Hagenaars, S. P., Davies, G., Wardlaw, J. M., Gale, C. R., Bastin, M. E., & Deary, I. J. (2016). Ageing and brain white matter structure in 3,513 UK Biobank participants. *Nature Communications*, *7*(1), 13629. https://doi.org/10.1038/ncomms13629

Davis, S. W., Dennis, N. A., Buchler, N. G., White, L. E., Madden, D. J., & Cabeza, R. (2009). Assessing the effects of age on long white matter tracts using diffusion tensor tractography. *NeuroImage*, *46*(2), 530–541. https://doi.org/10.1016/j.neuroimage.2009.01.068

de Groot, M., Cremers, L. G. M., Ikram, M. A., Hofman, A., Krestin, G. P., van der Lugt, A., Niessen, W. J., & Vernooij, M. W. (2016). White Matter Degeneration with Aging: Longitudinal Diffusion MR Imaging Analysis. *Radiology*, *279*(2), 532–541. https://doi.org/10.1148/radiol.2015150103

de Lange, A.-M., Barth, C., Kaufmann, T., Maximov, I. I., van der Meer, D., Agartz, I., & Westlye, L. T. (2019). *Cumulative estrogen exposure, APOE genotype, and women's*

brain aging—A population-based neuroimaging study [Preprint]. Neuroscience. https://doi.org/10.1101/826123

de Lange, A.-M. G., Kaufmann, T., van der Meer, D., Maglanoc, L. A., Alnæs, D., Moberget, T., Douaud, G., Andreassen, O. A., & Westlye, L. T. (2019). Population-based neuroimaging reveals traces of childbirth in the maternal brain. *Proceedings of the National Academy of Sciences*, *116*(44), 22341–22346. https://doi.org/10.1073/pnas.1910666116

De Santis, S., Gabrielli, A., Palombo, M., Maraviglia, B., & Capuani, S. (2011). Non-Gaussian diffusion imaging: A brief practical review. *Magnetic Resonance Imaging*, *29*(10), 1410–1416. https://doi.org/10.1016/j.mri.2011.04.006

Fieremans, E., Jensen, J. H., & Helpern, J. A. (2011). White matter characterization with diffusional kurtosis imaging. *NeuroImage*, *58*(1), 177–188. https://doi.org/10.1016/j.neuroimage.2011.06.006

Franke, K., Ziegler, G., Klöppel, S., & Gaser, C. (2010). Estimating the age of healthy subjects from T1-weighted MRI scans using kernel methods: Exploring the influence of various parameters. *NeuroImage*, *50*(3), 883–892. https://doi.org/10.1016/j.neuroimage.2010.01.005

Glover, S., & Dixon, P. (2004). Likelihood ratios: A simple and flexible statistic for empirical psychologists. *Psychonomic Bulletin & Review*, *11*(5), 791–806. https://doi.org/10.3758/BF03196706

Hope, T. R., Selnes, P., Rektorová, I., Anderkova, L., Nemcova-Elfmarkova, N., Balážová, Z., Dale, A., Bjørnerud, A., & Fladby, T. (2019). Diffusion tensor and restriction spectrum imaging reflect different aspects of neurodegeneration in Parkinson's disease. *PLOS ONE*, *14*(5), e0217922. https://doi.org/10.1371/journal.pone.0217922

Hua, K., Zhang, J., Wakana, S., Jiang, H., Li, X., Reich, D. S., Calabresi, P. A., Pekar, J. J., van Zijl, P. C. M., & Mori, S. (2008). Tract probability maps in stereotaxic spaces:

723 Analyses of white matter anatomy and tract-specific quantification. *NeuroImage*, *39*(1),
724 336–347. https://doi.org/10.1016/j.neuroimage.2007.07.053
725 Jbabdi, S., & Johansen-Berg, H. (2011). Tractography: Where Do We Go from Here? *Brain*
726 *Connectivity*, *1*(3), 169–183. https://doi.org/10.1089/brain.2011.0033
727 Jbabdi, S., Sotiropoulos, S. N., Savio, A. M., Graña, M., & Behrens, T. E. J. (2012). Model-
728 based analysis of multishell diffusion MR data for tractography: How to get over fitting
729 problems. *Magnetic Resonance in Medicine*, *68*(6), 1846–1855.
730 https://doi.org/10.1002/mrm.24204
731 Jelescu, I. O., & Budde, M. D. (2017). Design and Validation of Diffusion MRI Models of
732 White Matter. *Frontiers in Physics*, *5*, 61. https://doi.org/10.3389/fphy.2017.00061
733 Jelescu, I. O., Veraart, J., Adisetiyo, V., Milla, S. S., Novikov, D. S., & Fieremans, E. (2015).
734 One diffusion acquisition and different white matter models: How does microstructure
735 change in human early development based on WMTI and NODDI? *NeuroImage*, *107*,
736 242–256. https://doi.org/10.1016/j.neuroimage.2014.12.009
737 Jenkinson, M., Beckmann, C. F., Behrens, T. E. J., Woolrich, M. W., & Smith, S. M. (2012).
738 FSL. *NeuroImage*, *62*(2), 782–790. https://doi.org/10.1016/j.neuroimage.2011.09.015
739 Jensen, J. H., Helpern, J. A., Ramani, A., Lu, H., & Kaczynski, K. (2005). Diffusional kurtosis
740 imaging: The quantification of non-gaussian water diffusion by means of magnetic
741 resonance imaging. *Magnetic Resonance in Medicine*, *53*(6), 1432–1440.
742 https://doi.org/10.1002/mrm.20508
743 Kaden, E., Kelm, N. D., Carson, R. P., Does, M. D., & Alexander, D. C. (2016). Multi-
744 compartment microscopic diffusion imaging. *NeuroImage*, *139*, 346–359.
745 https://doi.org/10.1016/j.neuroimage.2016.06.002
746 Kaden, E., Kruggel, F., & Alexander, D. C. (2016). Quantitative mapping of the per-axon
747 diffusion coefficients in brain white matter: Quantitative Mapping of the Per-Axon

Diffusion Coefficients. *Magnetic Resonance in Medicine*, *75*(4), 1752–1763. https://doi.org/10.1002/mrm.25734

Kaufmann, T., van der Meer, D., Doan, N. T., Schwarz, E., Lund, M. J., Agartz, I., Alnæs, D., Barch, D. M., Baur-Streubel, R., Bertolino, A., Bettella, F., Beyer, M. K., Bøen, E., Borgwardt, S., Brandt, C. L., Buitelaar, J., Celius, E. G., Cervenka, S., Conzelmann, A., … Westlye, L. T. (2019). Common brain disorders are associated with heritable patterns of apparent aging of the brain. *Nature Neuroscience*, *22*(10), 1617–1623. https://doi.org/10.1038/s41593-019-0471-7

Kellner, E., Dhital, B., Kiselev, V. G., & Reisert, M. (2016). Gibbs-ringing artifact removal based on local subvoxel-shifts. *Magnetic Resonance in Medicine*, *76*(5), 1574–1581. https://doi.org/10.1002/mrm.26054

Krogsrud, S. K., Fjell, A. M., Tamnes, C. K., Grydeland, H., Mork, L., Due-Tønnessen, P., Bjørnerud, A., Sampaio-Baptista, C., Andersson, J., Johansen-Berg, H., & Walhovd, K. B. (2016). Changes in white matter microstructure in the developing brain—A longitudinal diffusion tensor imaging study of children from 4 to 11 years of age. *NeuroImage*, *124*, 473–486. https://doi.org/10.1016/j.neuroimage.2015.09.017

Lampinen, B., Szczepankiewicz, F., Mårtensson, J., van Westen, D., Sundgren, P. C., & Nilsson, M. (2017). Neurite density imaging versus imaging of microscopic anisotropy in diffusion MRI: A model comparison using spherical tensor encoding. *NeuroImage*, *147*, 517–531. https://doi.org/10.1016/j.neuroimage.2016.11.053

Le, T. T., Kuplicki, R. T., McKinney, B. A., Yeh, H.-W., Thompson, W. K., Paulus, M. P., & Tulsa 1000 Investigators. (2018). A Nonlinear Simulation Framework Supports Adjusting for Age When Analyzing BrainAGE. *Frontiers in Aging Neuroscience*, *10*, 317. https://doi.org/10.3389/fnagi.2018.00317

Likitjaroen, Y., Meindl, T., Friese, U., Wagner, M., Buerger, K., Hampel, H., & Teipel, S. J. (2012). Longitudinal changes of fractional anisotropy in Alzheimer's disease patients

treated with galantamine: A 12-month randomized, placebo-controlled, double-blinded study. *European Archives of Psychiatry and Clinical Neuroscience*, *262*(4), 341–350. https://doi.org/10.1007/s00406-011-0234-2

Lindenberger, U. (2014). Human cognitive aging: Corriger la fortune? *Science*, *346*(6209), 572–578. https://doi.org/10.1126/science.1254403

Maximov, I. I., Alnæs, D., & Westlye, L. T. (2019). Towards an optimised processing pipeline for diffusion magnetic resonance imaging data: Effects of artefact corrections on diffusion metrics and their age associations in UK Biobank. *Human Brain Mapping*, *40*(14), 4146–4162. https://doi.org/10.1002/hbm.24691

Maximov, I. I., Thönneßen, H., Konrad, K., Amort, L., Neuner, I., & Shah, N. J. (2015). Statistical Instability of TBSS Analysis Based on DTI Fitting Algorithm: TBSS analysis. *Journal of Neuroimaging*, *25*(6), 883–891. https://doi.org/10.1111/jon.12215

Maximov, I. I., van der Meer, D., de Lange, A.-M., Kaufmann, T., Shadrin, A., Frei, O., Wolfers, T., & Westlye, L. T. (2020). *Fast qualit **Y** con **T** rol me **T** hod fo **R** der **I** ved diff **U** sion **M** etrics (**YTTRIUM**) in big data analysis: UK Biobank 18608 example* [Preprint]. Neuroscience. https://doi.org/10.1101/2020.02.17.952697

Nilsson, M., Lätt, J., Ståhlberg, F., Westen, D., & Hagslätt, H. (2012). The importance of axonal undulation in diffusion MR measurements: A Monte Carlo simulation study: THE IMPORTANCE OF AXONAL UNDULATION IN DIFFUSION MR MEASUREMENTS. *NMR in Biomedicine*, *25*(5), 795–805. https://doi.org/10.1002/nbm.1795

Novikov, D. S., Fieremans, E., Jespersen, S. N., & Kiselev, V. G. (2019). Quantifying brain microstructure with diffusion MRI: Theory and parameter estimation. *NMR in Biomedicine*, *32*(4), e3998. https://doi.org/10.1002/nbm.3998

Pines, A. R., Cieslak, M., Larsen, B., Baum, G. L., Cook, P. A., Adebimpe, A., Dávila, D. G., Elliott, M. A., Jirsaraie, R., Murtha, K., Oathes, D. J., Piiwaa, K., Rosen, A. F. G.,

Rush, S., Shinohara, R. T., Bassett, D. S., Roalf, D. R., & Satterthwaite, T. D. (2020). Leveraging multi-shell diffusion for studies of brain development in youth and young adulthood. *Developmental Cognitive Neuroscience*, *43*, 100788. https://doi.org/10.1016/j.dcn.2020.100788

Racine, A. M., Merluzzi, A. P., Adluru, N., Norton, D., Koscik, R. L., Clark, L. R., Berman, S. E., Nicholas, C. R., Asthana, S., Alexander, A. L., Blennow, K., Zetterberg, H., Kim, W. H., Singh, V., Carlsson, C. M., Bendlin, B. B., & Johnson, S. C. (2019). Association of longitudinal white matter degeneration and cerebrospinal fluid biomarkers of neurodegeneration, inflammation and Alzheimer's disease in late-middle-aged adults. *Brain Imaging and Behavior*, *13*(1), 41–52. https://doi.org/10.1007/s11682-017-9732-9

Richard, G., Kolskår, K., Sanders, A.-M., Kaufmann, T., Petersen, A., Doan, N. T., Monereo Sánchez, J., Alnæs, D., Ulrichsen, K. M., Dørum, E. S., Andreassen, O. A., Nordvik, J. E., & Westlye, L. T. (2018). Assessing distinct patterns of cognitive aging using tissue-specific brain age prediction based on diffusion tensor imaging and brain morphometry. *PeerJ*, *6*, e5908. https://doi.org/10.7717/peerj.5908

Roalf, D. R., Quarmley, M., Elliott, M. A., Satterthwaite, T. D., Vandekar, S. N., Ruparel, K., Gennatas, E. D., Calkins, M. E., Moore, T. M., Hopson, R., Prabhakaran, K., Jackson, C. T., Verma, R., Hakonarson, H., Gur, R. C., & Gur, R. E. (2016). The impact of quality assurance assessment on diffusion tensor imaging outcomes in a large-scale population-based cohort. *NeuroImage*, *125*, 903–919. https://doi.org/10.1016/j.neuroimage.2015.10.068

Rueckert, D., Sonoda, L. I., Hayes, C., Hill, D. L. G., Leach, M. O., & Hawkes, D. J. (1999). Nonrigid registration using free-form deformations: Application to breast MR images. *IEEE Transactions on Medical Imaging*, *18*(8), 712–721. https://doi.org/10.1109/42.796284

Schaie, K. W. (2005). What Can We Learn From Longitudinal Studies of Adult Development? *Research in Human Development*, *2*(3), 133–158. https://doi.org/10.1207/s15427617rhd0203_4

Sexton, C. E., Walhovd, K. B., Storsve, A. B., Tamnes, C. K., Westlye, L. T., Johansen-Berg, H., & Fjell, A. M. (2014). Accelerated Changes in White Matter Microstructure during Aging: A Longitudinal Diffusion Tensor Imaging Study. *Journal of Neuroscience*, *34*(46), 15425–15436. https://doi.org/10.1523/JNEUROSCI.0203-14.2014

Smith, S. M. (2002). Fast robust automated brain extraction. *Human Brain Mapping*, *17*(3), 143–155. https://doi.org/10.1002/hbm.10062

Smith, S. M., Elliott, L. T., Alfaro-Almagro, F., McCarthy, P., Nichols, T. E., Douaud, G., & Miller, K. L. (2019). *Brain aging comprises multiple modes of structural and functional change with distinct genetic and biophysical associations* [Preprint]. Neuroscience. https://doi.org/10.1101/802686

Smith, S. M., Jenkinson, M., Johansen-Berg, H., Rueckert, D., Nichols, T. E., Mackay, C. E., Watkins, K. E., Ciccarelli, O., Cader, M. Z., Matthews, P. M., & Behrens, T. E. J. (2006). Tract-based spatial statistics: Voxelwise analysis of multi-subject diffusion data. *NeuroImage*, *31*(4), 1487–1505. https://doi.org/10.1016/j.neuroimage.2006.02.024

Smith, S. M., Jenkinson, M., Woolrich, M. W., Beckmann, C. F., Behrens, T. E. J., Johansen-Berg, H., Bannister, P. R., De Luca, M., Drobnjak, I., Flitney, D. E., Niazy, R. K., Saunders, J., Vickers, J., Zhang, Y., De Stefano, N., Brady, J. M., & Matthews, P. M. (2004). Advances in functional and structural MR image analysis and implementation as FSL. *NeuroImage*, *23*, S208–S219. https://doi.org/10.1016/j.neuroimage.2004.07.051

Smith, S. M., & Nichols, T. E. (2018). Statistical Challenges in “Big Data” Human Neuroimaging. *Neuron*, *97*(2), 263–268. https://doi.org/10.1016/j.neuron.2017.12.018

Smith, S. M., Vidaurre, D., Alfaro-Almagro, F., Nichols, T. E., & Miller, K. L. (2019). Estimation of brain age delta from brain imaging. *NeuroImage*, *200*, 528–539. https://doi.org/10.1016/j.neuroimage.2019.06.017

Smith, S., & Nichols, T. (2009). Threshold-free cluster enhancement: Addressing problems of smoothing, threshold dependence and localisation in cluster inference. *NeuroImage*, *44*(1), 83–98. https://doi.org/10.1016/j.neuroimage.2008.03.061

Storsve, A. B., Fjell, A. M., Yendiki, A., & Walhovd, K. B. (2016). Longitudinal Changes in White Matter Tract Integrity across the Adult Lifespan and Its Relation to Cortical Thinning. *PLOS ONE*, *11*(6), e0156770. https://doi.org/10.1371/journal.pone.0156770

Teipel, S. J., Meindl, T., Wagner, M., Stieltjes, B., Reuter, S., Hauenstein, K.-H., Filippi, M., Ernemann, U., Reiser, M. F., & Hampel, H. (2010). Longitudinal Changes in Fiber Tract Integrity in Healthy Aging and Mild Cognitive Impairment: A DTI Follow-Up Study. *Journal of Alzheimer's Disease*, *22*(2), 507–522. https://doi.org/10.3233/JAD-2010-100234

Tønnesen, S., Kaufmann, T., Doan, N. T., Alnæs, D., Córdova-Palomera, A., Meer, D. van der, Rokicki, J., Moberget, T., Gurholt, T. P., Haukvik, U. K., Ueland, T., Lagerberg, T. V., Agartz, I., Andreassen, O. A., & Westlye, L. T. (2018). White matter aberrations and age-related trajectories in patients with schizophrenia and bipolar disorder revealed by diffusion tensor imaging. *Scientific Reports*, *8*(1), 14129. https://doi.org/10.1038/s41598-018-32355-9

Veraart, J., Fieremans, E., & Novikov, D. S. (2016). Diffusion MRI noise mapping using random matrix theory. *Magnetic Resonance in Medicine*, *76*(5), 1582–1593. https://doi.org/10.1002/mrm.26059

Voldsbekk, I., Maximov, I. I., Zak, N., Roelfs, D., Geier, O., Due-Tønnessen, P., Elvsåshagen, T., Strømstad, M., Bjørnerud, A., & Groote, I. (2020). Evidence for wakefulness-related changes to extracellular space in human brain white matter from diffusion-

weighted MRI. *NeuroImage*, *212*, 116682. https://doi.org/10.1016/j.neuroimage.2020.116682

Westlye, L. T., Walhovd, K. B., Dale, A. M., Bjornerud, A., Due-Tonnessen, P., Engvig, A., Grydeland, H., Tamnes, C. K., Ostby, Y., & Fjell, A. M. (2010). Life-Span Changes of the Human Brain White Matter: Diffusion Tensor Imaging (DTI) and Volumetry. *Cerebral Cortex*, *20*(9), 2055–2068. https://doi.org/10.1093/cercor/bhp280

White, N. S., Leergaard, T. B., D'Arceuil, H., Bjaalie, J. G., & Dale, A. M. (2013). Probing tissue microstructure with restriction spectrum imaging: Histological and theoretical validation. *Human Brain Mapping*, *34*(2), 327–346. https://doi.org/10.1002/hbm.21454

Wilks, S. S. (1938). The Large-Sample Distribution of the Likelihood Ratio for Testing Composite Hypotheses. *The Annals of Mathematical Statistics*, *9*(1), 60–62. https://doi.org/10.1214/aoms/1177732360

Winkler, A. M., Ridgway, G. R., Webster, M. A., Smith, S. M., & Nichols, T. E. (2014). Permutation inference for the general linear model. *NeuroImage*, *92*, 381–397. https://doi.org/10.1016/j.neuroimage.2014.01.060

Yap, Q. J., Teh, I., Fusar-Poli, P., Sum, M. Y., Kuswanto, C., & Sim, K. (2013). Tracking cerebral white matter changes across the lifespan: Insights from diffusion tensor imaging studies. *Journal of Neural Transmission*, *120*(9), 1369–1395. https://doi.org/10.1007/s00702-013-0971-7

Zhang, H., Schneider, T., Wheeler-Kingshott, C. A., & Alexander, D. C. (2012). NODDI: Practical in vivo neurite orientation dispersion and density imaging of the human brain. *NeuroImage*, *61*(4), 1000–1016. https://doi.org/10.1016/j.neuroimage.2012.03.072

Zimmerman, D. W. (n.d.). *Correcting Two-Sample z and t Tests for Correlation: An Alternative to One-Sample Tests on Difference Scores*. 28.